Small-scale convective turbulence constrains microbial patchiness.

A. K. Christensen[1], M. D. Piggott[2], E. van Sebille[3], M. van Reeuwijk[4], S. Pawar[1]

[1]Department of Life Sciences, Imperial College London, UK

[2]Department of Earth Science and Engineering, Imperial College London, UK

[3]Utrecht University, The Netherlands

[4]Department of Civil and Environmental Engineering, Imperial College London, UK

Supplementary Information

Contents

1 Timestepping & numerical accuracy in the microbe IBM

The buoyancy-driven DNS offers a level of spatial granularity and complexity in the velocity fields that poses technical challenges for accurate particle tracking. If the choice of timestep is too small, the computational cost of the microbe IBM will be too great; if the timestep is too large then particles will move too far a distance in a single timestep, ignoring too much of the velocity field as they do so. We establish a sensible upper bound for the timestep using the Courant-Friedrichs-Lewy (CFL) condition.

The CFL condition provides a method for determining a maximal timestep without risking the introduction of inaccuracies or instabilities in an explicit time-integration scheme. The essential principle is to ensure that we do not allow particles to traverse a distance much greater than the separation of gridpoints in a single timestep. In the 3D case (and noting that in our case $\Delta x = \Delta y = \Delta z$) we can express this mathematically as:

$$\Delta t_{\text{cfl}} \left(\frac{|u_x| + |u_y| + |u_z|}{\Delta x} \right) \lesssim 1,$$

where u_x, u_y, u_z are the velocities in the x, y and z directions respectively. One particularly conservative approach is to determine the maximum values of $|u_x|, |u_y|, |u_z|$ across all timesteps in the DNS and all cells, to obtain an IBM timestep with which no particle in any cell or at any time will violate the CFL condition (the analysis for motile particles is the same as for non-motile particle since the maximum fluid velocities are much greater than the maximum swim speed of our particles). For the simulations considered in this work this yields the following:

$$\Delta x = 0.000\overline{833}m \qquad \text{and} \qquad \begin{bmatrix} \max(|u_x|) \\ \max(|u_y|) \\ \max(|u_z|) \end{bmatrix} = \begin{bmatrix} 0.16472499 \\ 0.1493763 \\ 0.1672444 \end{bmatrix} \text{m}\,\text{s}^{-1},$$

$$\implies \Delta t_{\text{cfl}} \leq \frac{0.000\overline{833}}{0.48134569}\text{s} \approx 0.0017\,\text{s}.$$

This is an extremely small timestep, requiring over 35,000 iterations to track particles through the full 60 seconds of each simulation. Recall, though, that this value of Δt would ensure that not a single one of our particles would violate the CFL condition in any cell or at any timestep. We do not require this level of conservatism because we will be simulating large numbers of particles – as long as the per-timestep error remains small, and sufficiently few particles are consistently found in cells with velocities as high as $\max(u_x)$, $\max(u_y)$ or $\max(u_z)$, then we can employ a larger timestep without particle trajectories erring significantly. Below we demonstrate that an IBM timestep of $\Delta t = 0.01\,\mathrm{s}$ is sufficient.

First consider the per-timestep error resulting from a switch to this new timestep. We ran two independent simulations for a total time of 0.1 s, each with 10,000 particles in identical initial positions, and with $\Delta t = 0.01\,\mathrm{s}$ and $\Delta t = 0.001\,\mathrm{s}$ respectively. The latter is less than Δt_{cfl}, and therefore will yield results at least as accurate as Δt_{cfl}, and was chosen to simplify the following analysis. For each of the 10,000 particles we compare the endpoints of their trajectories in the $\Delta t = 0.01\,\mathrm{s}$ and $\Delta t = 0.001\,\mathrm{s}$ simulations to obtain an estimate of the error we can expect per-timestep for a run with $\Delta t = 0.01\,\mathrm{s}$.

Supplementary Fig 1 shows a histogram and empirical cumulative distribution function (CDF) of the results, with mean marked as a vertical green line and 95%, 99% confidence limits marked as vertical red lines. We can see immediately that the per-timestep error is generally extremely small; confined in 95% of cases to $\leq 0.06\Delta x$, with the mean error at $0.01\Delta x$, and with only 1% of particles deviating by more than $0.09\Delta x$ per timestep.

How important is this 1% edge-case of per-timestep errors? If a particle consistently found itself this deep in the upper end of the per-timestep error distribution then its trajectory could become inaccurate over the course of the full 60 s simulation. How might a particle find itself in such a situation? The error at a given timestep t will be highest for the particles which find themselves in high-velocity cells at t, since this will mean that those in the $\Delta t = 0.01\,\mathrm{s}$ simulation may jump over several cells by the next timestep $t + 0.01\,\mathrm{s}$, whereas their Δt_{cfl} counterparts will sample much more precisely the velocity field on the many timesteps they take to reach $t + 0.01\,\mathrm{s}$. Let us therefore also examine the distribution of velocities in each cell during the full 60 s IBM simulation period, to see how often we might expect a particle to find itself in a high-velocity cell.

Supplementary Fig 2 shows a histogram and empirical CDF of this data, with mean marked as a vertical green line and 95%, 99% confidence limits marked as vertical red lines. We can see that the distribution is heavily skewed; mean cell velocity over all timesteps is $0.01\mathrm{m\,s^{-1}}$ and the fraction of data with velocities $\geq 0.07\mathrm{m\,s^{-1}}$ is only 1%. Indeed with a timestep of $\Delta t = 0.01\,\mathrm{s}$ and a cell side-length of $\Delta x = 0.000833\mathrm{m}$, only in this 1% of cells would particles find themselves moving far enough in one timestep to violate the CFL condition. We conclude that with a timestep of $\Delta t = 0.01\,\mathrm{s}$, DNS cells in which particles are at risk of violating the CFL condition are rare. Since such cells are those with the largest fluid velocities, particles encountering one will pass through rapidly, instead spending more time in low-velocity DNS cells where the CFL condition is safely met. Finally, we note that our analyses in this paper are concerned not with the final position of the particles given their initial position (i.e. not in the accumulated per-timestep errors by the end of the simulation), but rather in how the particles aggregate together and drift apart from each other as they move through the flow. The proposed $\Delta t = 0.01\,\mathrm{s}$ timestep is thus sufficient for our purposes.

2 Deardorff velocity scales: Translating from the DNS to real-world flows.

The computational cost of DNS prohibits the outright simulation of a 1:1 scale water column, even for computationally less costly turbulent regimes such as the homogeneous isotropic turbulent flows frequently employed in the literature[8, 9]. Nonetheless, well-understood scaling relationships allow us to demonstrate that the outcomes of to-scale experiments such as ours are robust and representative of expected behaviour even in larger, true-scale systems. Our fluid DNS models a small ($0.6\,\mathrm{m} \times 0.6\,\mathrm{m} \times 0.3\,\mathrm{m}$) cuboid representation of buoyancy-driven turbulence wherein buoyancy gradients (and thus induced turbulent fluid motion) rapidly decline with depth (see again Fig. 1). We found that, nearer the surface, intense turbulent fluid motion overpowered the swimming and reorienting capabilities of all our simulated motile microbes. In contrast, at greater depths with more quiescent waters,

the fluid motion was less intense and the most agile motile particles were able to attain the balance of viscous and stabilising torques needed to enable significant patch enhancement. What do fluid-dynamical scaling arguments tell us about interpreting these results in a real-world context? The convective velocity scale[1, 5] describes the dependency of the magnitude of turbulent velocity fluctuations on physical parameters of the flow in a 3D convective mixed layer and takes the following form:

$$w^* = \Big[Bh\Big]^{1/3}, \tag{1}$$

where h is the depth of the mixed layer and B is the surface buoyancy flux. To determine the ratio between velocity scales in a real-world context and in our simulated fluid, we need to compute the two velocity scales w^*_{DNS} and w^*_{real}. We will focus on comparison to oceanic conditions, for which reliable global datasets of the relevant physical parameters are available. In our DNS, the mixed layer depth h is approximately 0.15 m and the surface buoyancy flux $B = \beta g \phi$ is equal to $-5 \times 10^{-4}\,\mathrm{m^2\,s^{-3}}$, where $\phi = Q/\rho c_p$ is the surface temperature flux, Q is the surface heat flux, ρ is density, and c_p is specific heat capacity. Here the negative sign simply indicates that buoyancy is being lost to the atmosphere; we will use the absolute value of the fluxes in computing the velocity scales. Plugging these values into equation 1 yields:

$$w^*_{\mathrm{DNS}} = 0.042\,\mathrm{m\,s^{-1}}. \tag{2}$$

To determine velocity scale associated with a cooling oceanic context, we need the mixed-layer depth and surface buoyancy flux. Oceanic mixed layer depth varies widely with season, latitude and weather conditions. If we exclude polar and sub-polar regions (where ocean temperature profiles do not resemble that of our DNS – see again Fig. 1) to which our fluid simulation is not comparable, then upper and lower limits for the ocean mixed layer depth lie between 10–1000 m[3].

Global maps of mean air-sea buoyancy fluxes, converted to equivalent heat fluxes ($\mathrm{W\,m^{-2}}$) are published in [7, 2], and show large regions of the world's oceans with average flux in the range of -25 to $-150\,\mathrm{W\,m^{-2}}$, corresponding to cooling waters where heat is being lost to

the atmosphere. We converted these into a buoyancy flux ($\mathrm{m^2\,s^{-3}}$), assuming ocean surface temperatures in the range of 10 to 30 °C (again excluding very high latitudes where our fluid model is not appropriate) and salinity in the range of 20 to $40\,\mathrm{g\,kg^{-1}}$, and thus seawater densities and specific heat capacities of 1013.4 to $1028.8\,\mathrm{kg\,m^{-3}}$ and 3968.1 to $4078.3\,\mathrm{J\,K^{-1}}$ respectively[6, 4]. This yields oceanic buoyancy fluxes in the range of $B_{\mathrm{ocean}} = -6.04 \times 10^{-6}$ to $-3.68 \times 10^{-5}\,\mathrm{m^2\,s^{-3}}$. Applying equation 1 again yields:

$$0.039\,\mathrm{m\,s^{-1}} \lesssim w^*_{\mathrm{ocean}} \lesssim 0.33\,\mathrm{m\,s^{-1}}. \tag{3}$$

We can now compute the ratio of velocity scales to compare the magnitude of turbulent velocity fluctuations in our DNS to that expected in a 1:1 scale simulation, or a real fluid. This yields upper and lower bounds on the ratio of the convective velocity scales in our DNS and in comparable ocean waters undergoing convective mixing:

$$0.94 \lesssim \frac{w^*_{\mathrm{ocean}}}{w^*_{\mathrm{DNS}}} \lesssim 7.88. \tag{4}$$

We conclude that a real-world ocean mixed-layer with weak surface cooling and a shallow mixed layer depth has turbulent velocities of a very similar (though slightly smaller) scale to our DNS, while in a real-world scenario with stronger surface cooling and a deeper mixed layer, velocities may be up to ~ 8 times stronger. The greater (and more positive) the ratio of oceanic to DNS velocity scales, the more that the contribution of fluid advection to microbe transport will dominate over the contribution of gyrotactic motility, further suppressing patch enhancement relative to our simulations.

3 Supplementary Figures

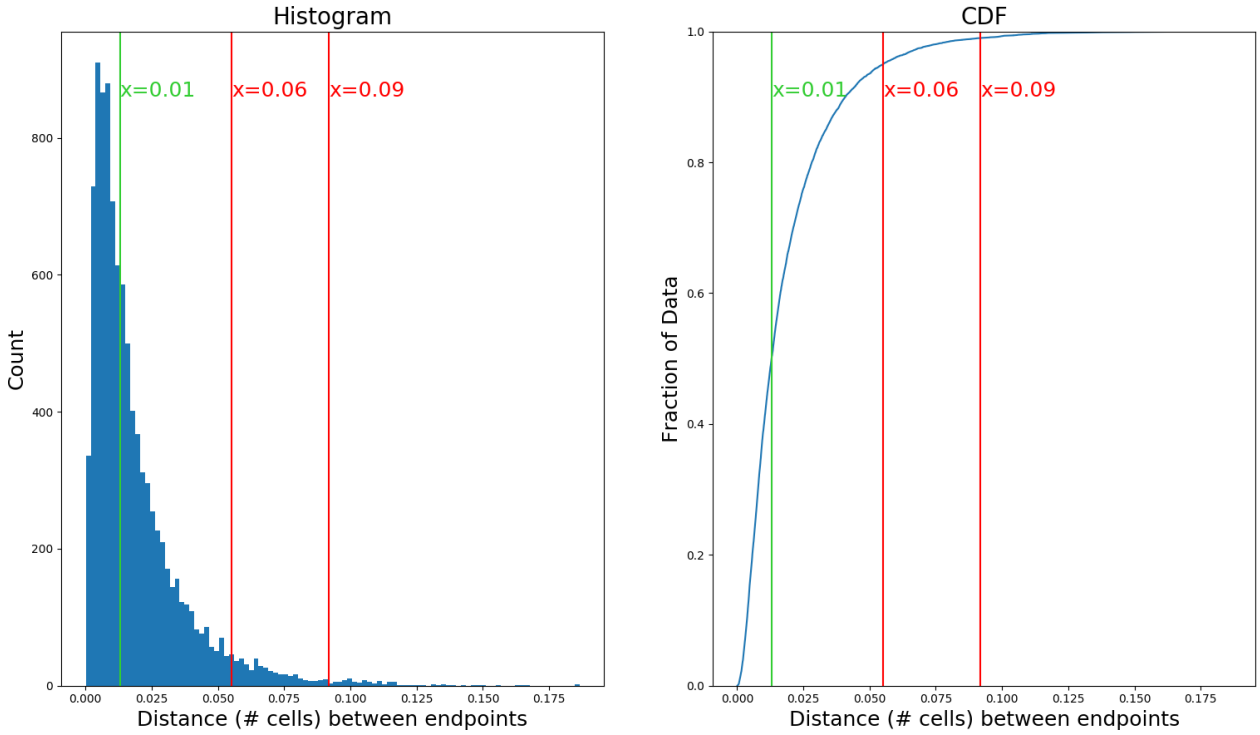

Supplementary Figure 1: Per-Timestep Error between $\Delta t = 0.01\,\mathrm{s}$ and $\Delta t = 0.001\,\mathrm{s}$. Mean marked as vertical green line, 95% and 99% confidence limits marked as vertical red lines.

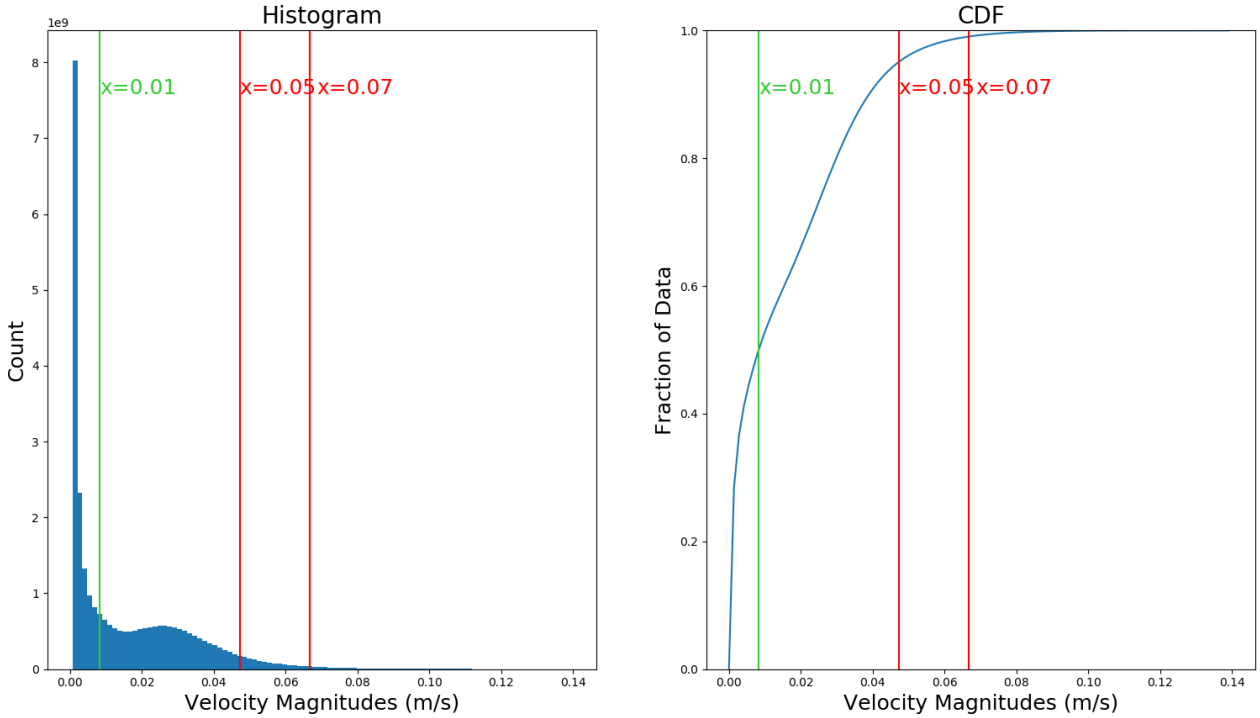

Supplementary Figure 2: Distribution of Cellwise Velocity Magnitudes across all timesteps. 95% and 99% confidence limits marked as vertical red lines. Mean marked as vertical green line, 95% and 99% confidence limits marked as vertical red lines.

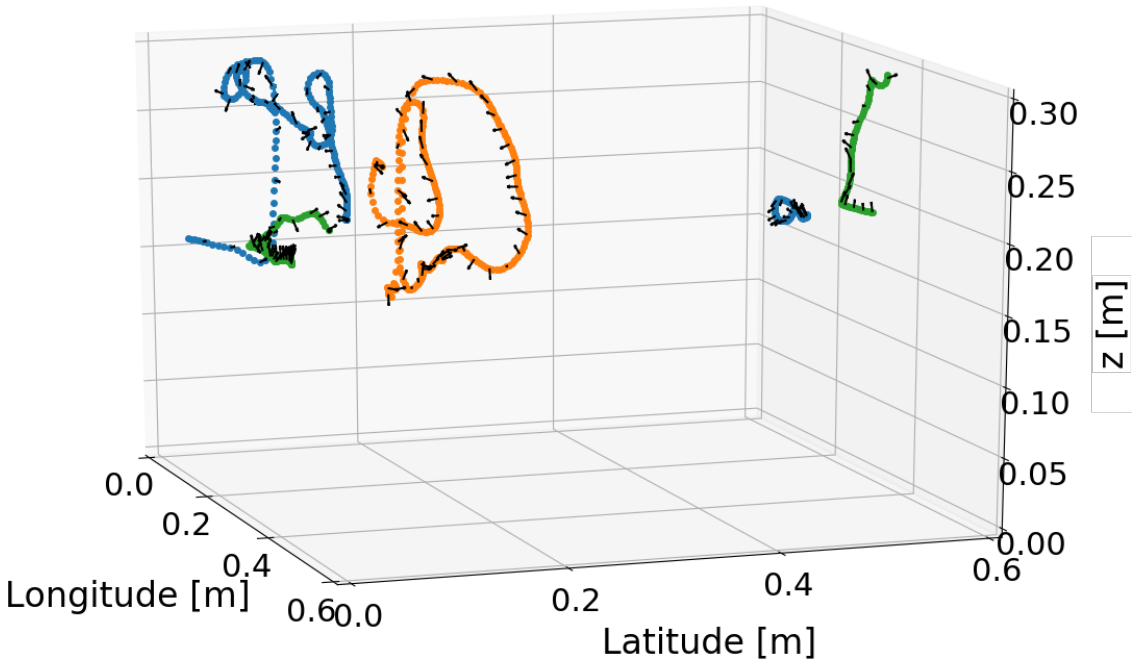

Supplementary Figure 3: Sample of 2 3D microbe trajectories with superimposed microbe orientations from $t = 0$–$30\,\mathrm{s}$ in the $(B, v_{\mathrm{swim}}) = (5\,\mathrm{s}, 10\,\mu\mathrm{m\,s^{-1}})$ motile simulation. Axes are labelled in units of DNS cell side-length. Each uniquely-coloured set of dots represents a single microbe's trajectory. Black arrows represent the instantaneous microbe orientation every $0.5\,\mathrm{s}$. Owing to the periodic boundaries in the longitudinal and latitudinal directions, trajectories may appear discontinuous when a microbe moves through such a boundary (e.g. green trajectory).

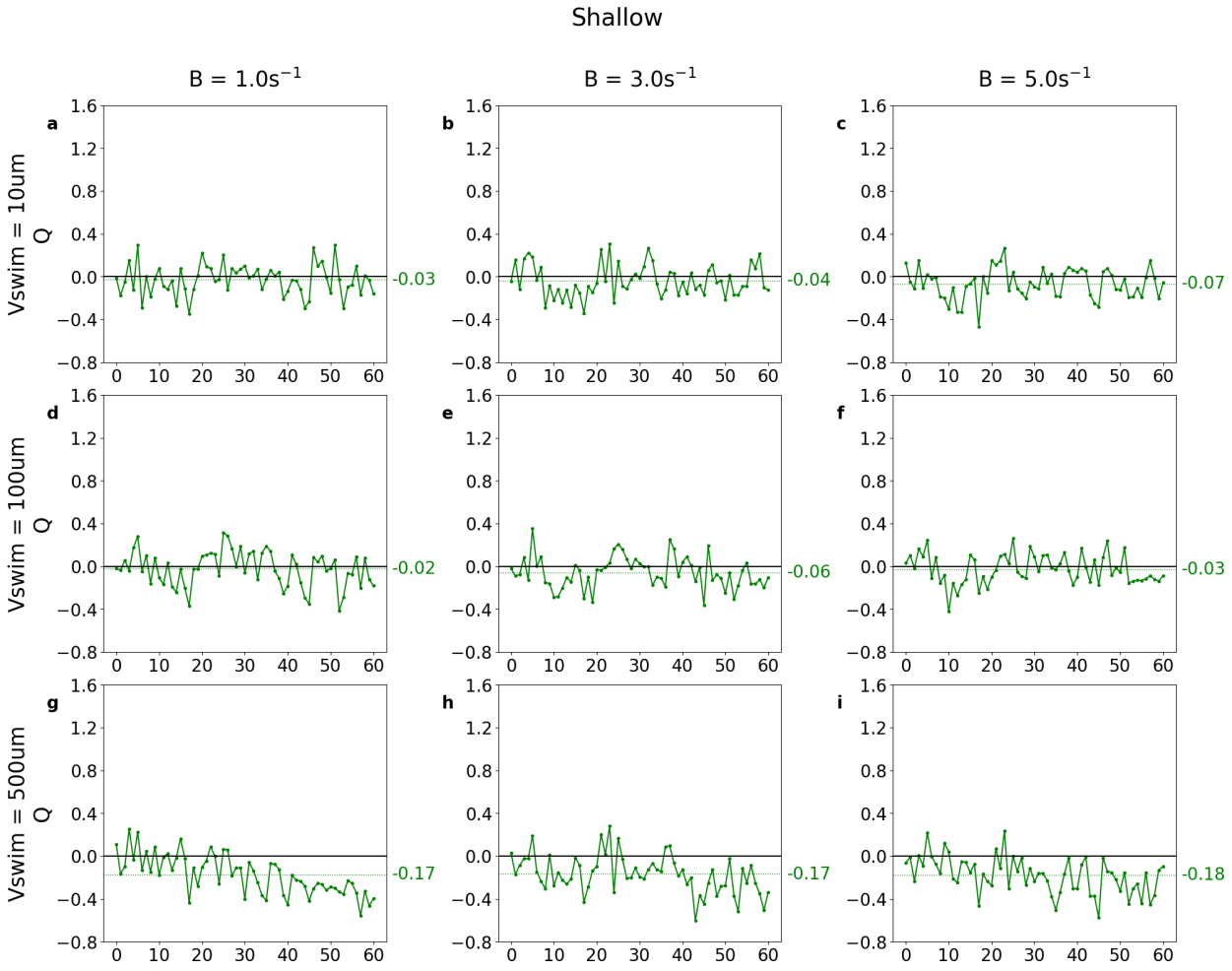

Supplementary Figure 4: Q-statistic over time (solid green line) and mean Q-statistic (dashed green line) for the 1% most aggregated cells in the Shallow region of each simulation.

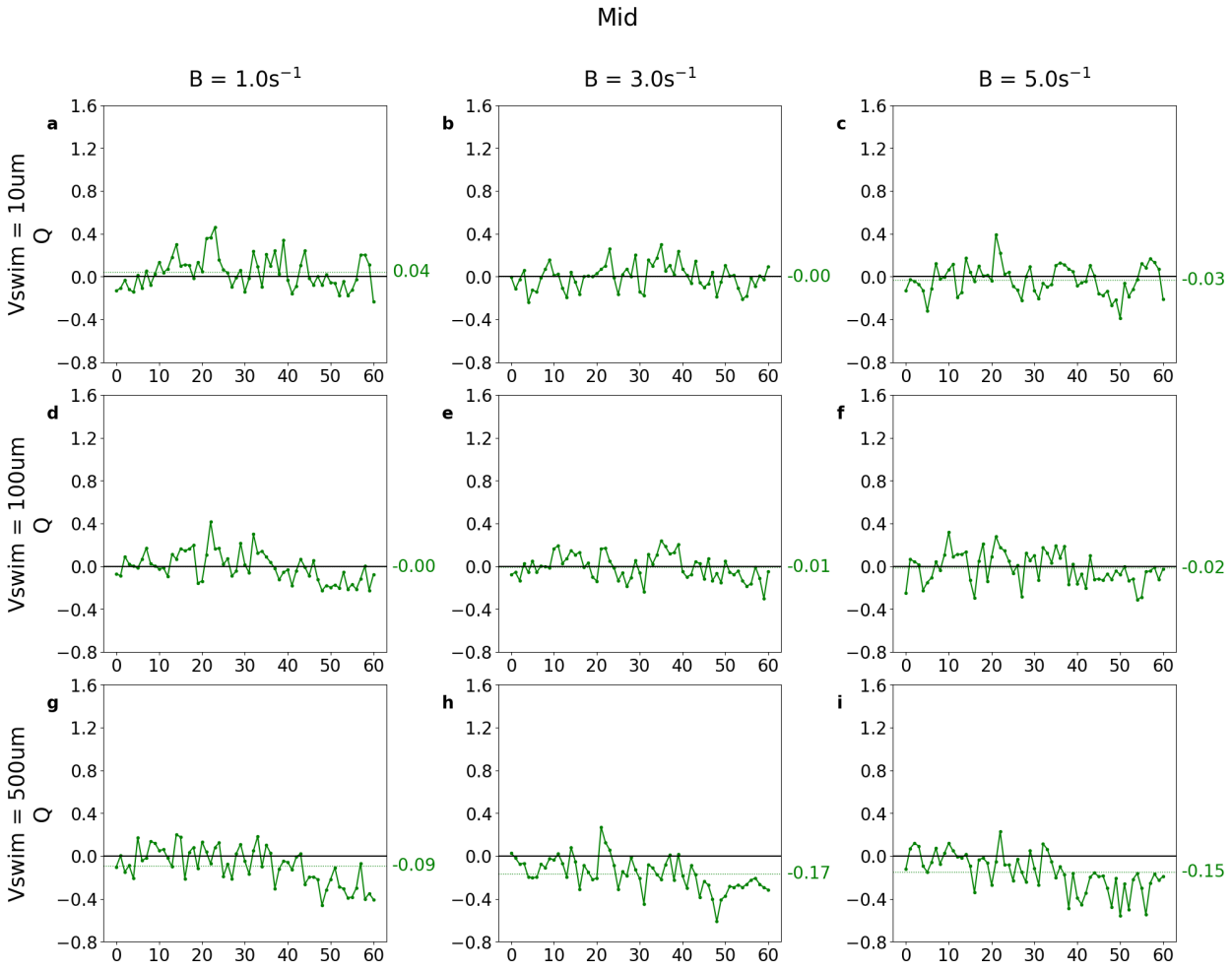

Supplementary Figure 5: Q-statistic over time (solid green line) and mean Q-statistic (dashed green line) for the 1% most aggregated cells in the Mid region of each simulation.

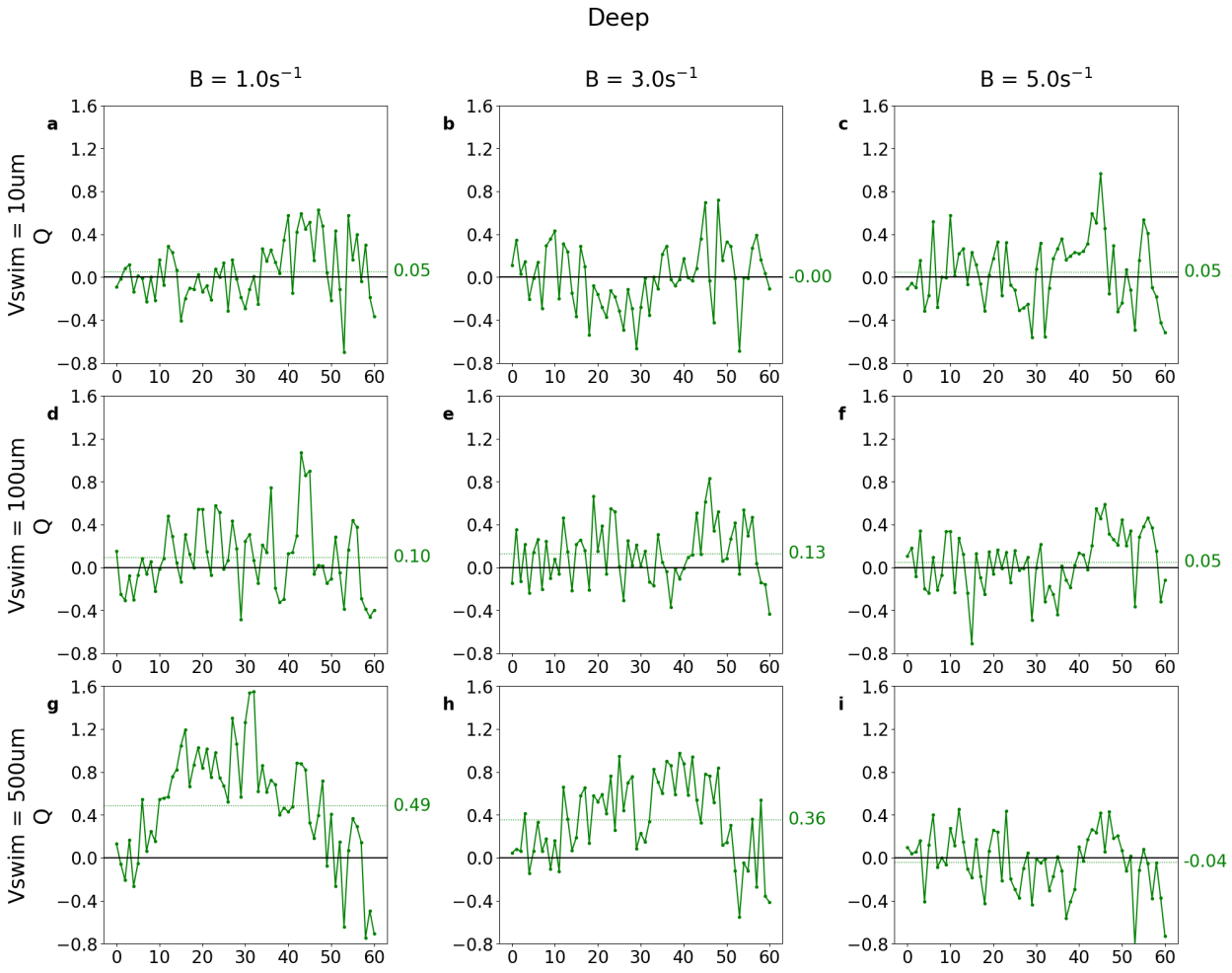

Supplementary Figure 6: Q-statistic over time (solid green line) and mean Q-statistic (dashed green line) for the 1% most aggregated cells in the Deep region of each simulation.

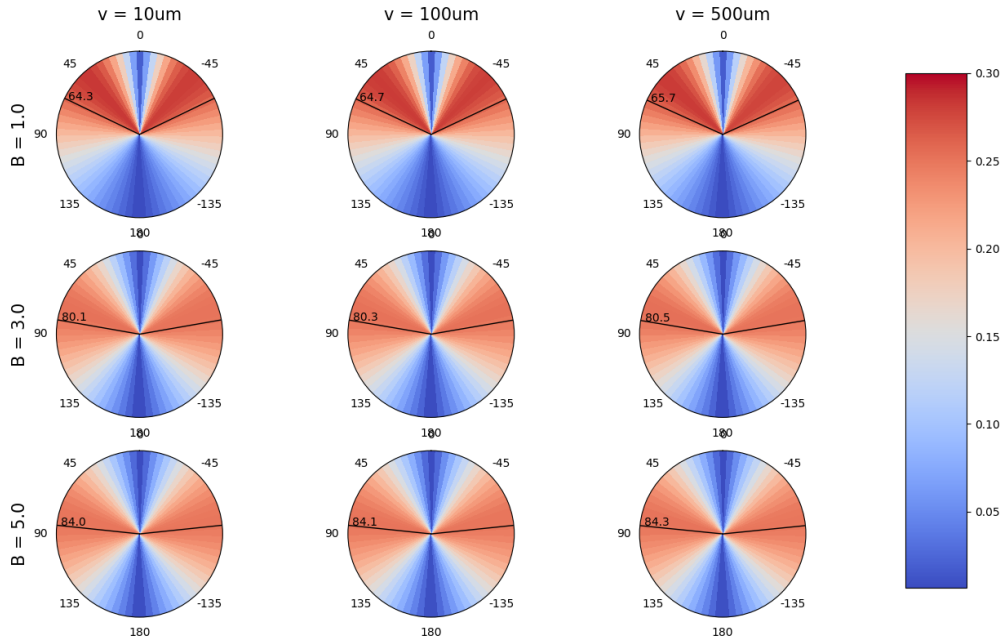

Supplementary Figure 7: Normalised distributions of polar angle of microbe orientation in each simulation.

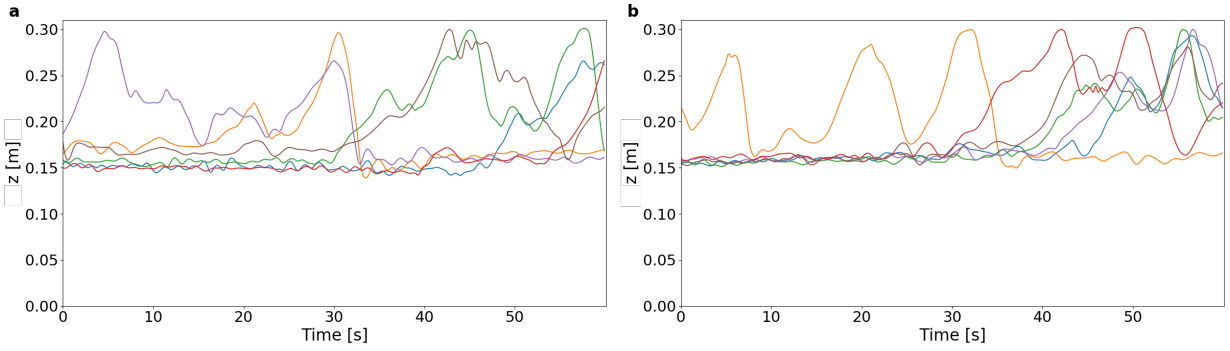

Supplementary Figure 8: A sample of 6 microbe depth trajectories in the **(a)** $(B, v_{\text{swim}}) = (5\,\text{s}, 10\,\mu\text{m}\,\text{s}^{-1})$ and **(b)** $(B, v_{\text{swim}}) = (1\,\text{s}, 500\,\mu\text{m}\,\text{s}^{-1})$ simulations, which exhibit rapid vertical movement due to transport in upwelling/downwelling fluid packets, along with exploratory sojourns in deeper, less turbulent regions.

References

[1] Deardorff, James W. *Convective Velocity and Temperature Scales for the Unstable Planetary Boundary Layer and for Rayleigh Convection.* Journal of the Atmospheric Sciences, 27:1211-1213, 1970.

[2] Large, W. G. and Yeager, S. G. *The global climatology of an interannually varying air-sea flux data set.* Climate Dynamics, 33(2):341-364, 2009.

[3] Montegut, Clement de Boyer and Madec, Gurvan and Fischer, Albert S. and Lazar, Alban and Iudicone, Daniele. *Mixed layer depth over the global ocean: An examination of profile data and a profile-based climatology.* Journal of Geophysical Research: Oceans, 109(C12), 2004.

[4] Nayar, Kishor G. and Sharqawy, Mostafa H. and Banchik, Leonardo D. and Lienhard V, John H. *Thermophysical properties of seawater: A review and new correlations that include pressure dependence.* Desalination, 390:1-24, 2016.

[5] Rutgersson, A. and Smedman, A. and Sahlee, E. *Oceanic convective mixing and the impact on air-sea gas transfer velocity.* Geophysical Research Letters, 38(2), 2011.

[6] Sharqawy, Mostafa H. and V, John H. Lienhard and Zubair, Syed M. *Thermophysical properties of seawater: a review of existing correlations and data.* Desalination and Water Treatment, 16(1-3):354-380, 2010.

[7] Talley, Lynne D. and Pickard, George L. and Emery, William J. and Swift, James H. *Descriptive Physical Oceanography (Sixth Edition)* Chapter 5 - Mass, Salt, and Heat Budgets and Wind Forcing, pp111-145. Academic Press, Cambridge, Massachussetts, 2011.

[8] Taylor, John R. and Stocker, R. *Trade-Offs of Chemotactic Foraging in Turbulent Water* Science, 338(6107):675-679, 2012.

[9] Watteaux, R. and Stocker, R. and Taylor, John R. *Sensitivity of the rate of nutrient uptake by chemotactic bacteria to physical and biological parameters in a turbulent environment* Journal of Theoretical Biology, 387:120-135, 2015.